Hwang, J., Walczak, R., Oschatz, M., Tarakina, N. V. and Schmidt, B. V.K.J. (2019) Micro-blooming: hierarchically porous nitrogen-doped carbon flowers derived from metal-organic mesocrystals. *Small*, 15(37), 1901986.

There may be differences between this version and the published version. You are advised to consult the publisher's version if you wish to cite from it.

This is the peer reviewed version of the following article Hwang, J., Walczak, R., Oschatz, M., Tarakina, N. V. and Schmidt, B. V.K.J. (2019) Micro-blooming: hierarchically porous nitrogen-doped carbon flowers derived from metal-organic mesocrystals. *Small*, 15(37), 1901986, which has been published in final form at http://dx.doi.org/10.1002/smll.201901986. This article may be used for non-commercial purposes in accordance with Wiley Terms and Conditions for Self-Archiving.

http://eprints.gla.ac.uk/190062/

Deposited on: 12 July 2019

**Micro-Blooming: Hierarchically Porous Nitrogen-doped Carbon Flowers derived from Metal-Organic Mesocrystals**

*Jongkook Hwang, Ralf Walczak, Martin Oschatz, Nadezda V. Tarakina, and Bernhard V. K. J. Schmidt\**

Dr. J. Hwang, R. Walczak, Dr. M. Oschatz, Dr. N. V. Tarakina, Dr. B. V. K. J. Schmidt
Department of Colloid Chemistry, Max-Planck Institute of Colloids and Interfaces, Am Mühlenberg 1, Potsdam, 14476, Germany
E-mail: bernhard.schmidt@mpikg.mpg.de

Dr. B. V. K. J. Schmidt
School of Chemistry, University of Glasgow, Glasgow G12 8QQ, UK

**Abstract**

Synthesis of 3D flower-like zinc-nitrilotriacetic acid (ZnNTA) mesocrystals and their conformal transformation to hierarchically porous N-doped carbon superstructures are reported. During the solvothermal reaction, 2D nanosheet primary building blocks undergo oriented attachment and mesoscale assembly forming stacked layers. The secondary nucleation and growth preferentially occur at the edges and defects of the layers, leading to formation of 3D flower-like mesocrystals comprised of interconnected 2D micropetals. By simply varying the pyrolysis temperature (550-1000 °C) and the removal method of in-situ generated Zn species, nonporous parent mesocrystals are transformed to hierarchically porous carbon flowers with controllable high surface area (970–1605 $m^2\,g^{-1}$), nitrogen content (3.4-14.1 at%), pore volume (0.95-2.19 $cm^3\,g^{-1}$), as well as pore diameter and structures. The carbon flowers prepared at 550 °C show high $CO_2/N_2$ selectivity due to the high nitrogen content and the large fraction of (ultra)micropores which can greatly increase the $CO_2$ affinity. The results show that the physicochemical properties of end-carbons are highly dependent on the thermal transformation and associated pore formation process, rather than directly inherited from parent precursors. The present strategy demonstrates metal-organic mesocrystals as a facile and versatile means

toward 3D hierarchical carbon superstructures that are attractive for a number of potential applications.

## 1. Introduction

Hierarchical carbon materials with defined 3-dimensional (3D) superstructure have attracted significant attention because of their unique textural properties that simultaneously combine the benefits of 3D assembled architectures and multiscale pore structures.[1-4] The 3D superstructure can inherit unique collective properties and a number of defect (active) sites arising from their subunit ensembles, which are otherwise difficult to realize.[4, 5] Micro/mesopores introduce a high surface area, a number of adsorption sites and size selectivity and macropores enhance the mass transport capability.[6-9] These advantageous features make hierarchical carbons attractive for a wide variety of applications such as adsorption, catalysis, and energy storage and conversion.[1, 9-14] For instance, flower-like carbon superstructures have been of particular interest in the field of electrocatalysis and energy storage. This is because of the high accessibility of the micro- and mesopores or catalytically active sites for the electrolyte provided by the unique morphology with a hierarchical pore structure and the facile electron transport through the 3D interconnected nanopetals, which leads to exceptional electrochemical performance.[15-24] Flower-like and hierarchical carbons in general have been prepared by using various low-dimensional building blocks (e.g., polymer sheets, carbon nanotubes, graphene oxide)[3, 4, 15, 20] and multiple templates with different length scales (e.g., block copolymers, silica materials, foams). [14, 16, 18, 19, 25, 26] However, the approaches usually rely on time-consuming and laborious multi-step procedures, including preparation of building blocks/sacrificial templates and their bottom-up assembly under specific conditions, infiltration/polymerization of carbon source, carbonization and template removal.[14, 25, 26] In addition, they sometimes need additional pore-forming agents or physical/chemical activation

2

to generate a hierarchical pore structure.[15, 18, 27] In this regard, development of a straightforward template-free approach toward hierarchically porous 3D carbon superstructures is highly desired.

Metal-organic coordination compounds, typically prepared by reacting metal salts with organic ligands, have shown promise as versatile precursors/templates for preparation of functional hierarchically porous carbons and their metal/metal oxide composites via a simple thermal transformation process.[28-30] Particular attention has been paid to crystalline metal-organic frameworks (MOFs) because of their highly ordered and chemically homogeneous structures, tunable pore size and large surface area, which are highly attractive features for fabricating advanced MOF-derived nanomaterials with tailored properties.[29, 31-37] For the past decade, considerable progress has been made in development of MOF-derived carbons (MDCs) suitable for a wide range of applications.[38-44] However, the macroscopic shapes of MDCs are mostly limited to simple cubic, rods, or hexagons that are inherited from characteristic morphology of MOF. In addition, the understanding of thermal transformation mechanisms and their effects on the physicochemical properties of the resulting carbons are still a matter of research.[45-48] Hence, it is highly desirable (i) to develop a new approach that enables synthesis of hierarchically porous carbon with a high level of morphological complexity other than simple (an)isotropic particle shape, and (ii) to understand underlying thermal transformation process to obtain carbons with desired porosity and physicochemical properties.

Recently, bioinspired synthesis of a new type of metal-organic coordination compounds, namely, metal-organic mesocrystals have been introduced.[49] Mesocrystals are a kind of superstructure comprised of crystalline nano/micro building blocks that are aligned in a crystallographic manner.[5, 50, 51] Natural organisms can create sophisticated multi-dimensional organic-inorganic hybrid mesocrystals via particle-mediated growth and assembly (i.e., nonclassical crystallization pathways), as observed in various biominerals such as bone, nacre, sea urchins and others.[50] Such particle-based crystallization is usually achieved by kinetic

control via organic additives (e.g., polymers, proteins) and often involves nanoparticle aggregation, self-assembly and mesoscopic transformation which can open new strategies for crystal morphogenesis. Indeed, coordination of metal ions by biomolecules has shown unique self-assembly behaviors that allow fabrication of multiscale architectures and complex morphologies.[52-55] In this regard, the use of bioinspired metal-organic mesocrystals as precursors can provide an unique opportunity to develop a new class of hierarchically structured carbon that may not be easily prepared by conventional templating methods and from MOF-based precursors. To date, synthesis of metal-organic mesocrystals and their transformation into functional nanomaterials remain largely unexplored.

Herein, we report the simple and template-free synthesis of a nitrogen-doped 3D carbon flowers with hierarchical pore architecture through direct thermal transformation of zinc-nitrilotriacetic acid (ZnNTA) mesocrystals (**Scheme 1**). ZnNTA mesocrystals are prepared by solvothermal reaction of zinc nitrate hexahydrate and NTA in dimethylformamide (DMF). The resulting structures are further subjected to carbonization under $N_2$ atmosphere and the effects of the pyrolysis temperature (550-1000 °C) as well as the role of in-situ generated Zn species on physicochemical properties (porosity, nitrogen content and configuration, degree of graphitization) of resulting carbon flowers are investigated. The selective adsorption of $CO_2$ in the presence of $N_2$ is studied in order to demonstrate the advantages of the control over the pore structures, which is achievable by controlling the synthesis temperature.

## 2. Results and Discussion

NTA is an artificially-made biomimetic chelating agent that has been widely used in various industrial applications such as detergents, metal-ion capture, and wastewater treatment.[56] Thus, NTA is an attractive candidate for cooperative self-assembly with metal ions[57] to form a new type of metal-NTA mesocrystal with unique particle morphologies. Indeed, flower-like ZnNTA mesocrystals were simply prepared by mixing Zn salt and NTA (Zn/NTA molar ratio

= 1.5) in HNO$_3$/DMF solution after solvothermal reaction at 120 °C for 24 h. Scanning electron microscopy (SEM) images show flower-like ZnNTA particles with a size of ~ 100 μm (**Figure 1**a). The micropetals interconnect each other and self-assemble to flower-like architectures. Higher magnification images show that each micropetal is constructed by small 2D nanosheets as building blocks, which is a typical characteristic of mesocrystals (Figure 1b, c). Transmission electron microscopy (TEM) reveals the randomly distributed mesopores originated from the defects and intraparticle voids of the mesocrystalline assembly (Figure 1d). Moreover, X-ray powder diffraction (XRD) shows the characteristic crystalline nature of ZnNTA crystals, which are totally different from the precursors used (**Figure S1**a). The formation of Zn-NTA coordination bonds was supported by Fourier-transform infrared (FT-IR) spectra (Figure S1b). After mesocrystal formation, an intense band at 1720 cm$^{-1}$ from the stretching vibration of C=O of carboxylic acids in NTA completely disappears, suggesting the successful coordination of Zn ion by NTA. ZnNTA mesocrystals have very low Brunauer–Emmett–Teller (BET) surface area of 7 m$^2$ g$^{-1}$ and a few mesopores ranging from 5-20 nm (Figure S1d).

The Zn/NTA molar ratio was varied from 1 to 1.5 to 2, to investigate its effect on crystal structure and morphology. Independent of the Zn/NTA ratio, ZnNTA crystals show flower-like morphologies (**Figure S2**a-c) and comparable XRD patterns (Figure S2d). All ZnNTAs also have similar thermal stability and materials composition, as confirmed by thermogravimetric analysis (TGA) conducted under artificial air flow (Figure S2e). The estimated materials composition from TGA is Zn/NTA = 1.5 in all samples, corresponding to the coordination number to achieve an electroneutral framework. The results indicate that flower-like ZnNTA mesocrystals with almost the same composition and structures are obtained regardless of the Zn/NTA ratio used for synthesis.

The kinetic control of crystallization can provide new opportunities for investigating the crystal growth process/mechanism and for preparing the crystals with high level of structural hierarchies.[49, 58] For these purposes, here we used HNO$_3$ as an additive that hinders the

5

deprotonation of NTA ligand, and thus affects the kinetics of the nucleation and growth (**Figure 2**). The effect of $HNO_3$ concentration on the size and morphology of ZnNTA was investigated by changing the molar ratio $r$ = $HNO_3$/NTA under the same solvothermal reaction for 24 h. In the absence of $HNO_3$, tetragonal 2D nanosheets with the approximate size/thickness of 200/10 nm were prepared (Figure 2a). At $r$ = 1, multilayer stacked particles comprised of such 2D nanosheets were observed (Figure 2b, c). 3D flower-like structures were generated at $r$ = 2 (Figure 2d), and became larger with an increase of $HNO_3$ ($r$ = 3) (Figure 2e). Further increase of $HNO_3$ considerably inhibits the crystal growth and assembly, and thus leads to formation of some nanocrystals ($r$ = 4.5) and even amorphous aggregates ($r$ = 6) (**Figure S3**). XRD diffractions become more intense with an increase of $r$ from 1 to 3, possibly due to the increase in crystallinity and the alignment of 2D nanosheets in the $c$-direction (Figure 2f). Thus, $HNO_3$ plays a crucial role in preparation of flower mesocrystals, as $HNO_3$ retards the deprotonation of NTA and by that lowers the rate of nucleation induced by coordination of NTA with Zn ions. With increasing amount of $HNO_3$, fewer nuclei are generated and grew to larger crystals. As the nucleation was largely retarded by $HNO_3$, secondary heterogeneous nucleation can continuously occur at the defect sites of the preformed layers,[59] which results in formation of 3D flower assemblies comprised of 2D layers.

To gain further insights on crystal growth process, time dependent ex-situ SEM studies were conducted for the flower mesocrystals prepared under the standard synthesis conditions (Zn/NTA = 1.5 and $HNO_3$/NTA = 3) (**Figure S4**). The initial reactant solution is homogeneous and transparent without any precipitates. The flower-like mesocrystal can only be prepared after solvothermal reaction at 120 °C. The stacked-microsheets emerge at the early stage of reaction for 4h (Figure S4a, b), and steadily self-assemble to flower-like particles after 6h. Newly formed nanosheets and branches grow on the surface and at the edges of the preformed layers, which can generate the curvature of the initially stacked layers (Figure S4c, d). Further growth

and development of new layers result in the formation of flower-shaped mesocrystals with a number of extended micropetals interconnecting each other (Figure S4e-h).

Based on these results, we suggest the formation mechanism of 3D flower ZnNTA mesocrystals (Figure 2g), i.e., the mesoscale assembly via oriented attachment[60] and the secondary nucleation and growth on the preformed layers. The mesocrystal growth proceeds step-by-step in a hierarchical way. At first, the 2D nanosheets – the primary building blocks – are generated, and subsequently self-aggregate along the common crystallographic basal- and edge-plane via oriented attachment to reduce the total surface energy of the system, thereby building up the secondary stacked layers with several micrometer size. As the size of those particles increases, the number of defects originated from mesoscale assembly increases significantly.[61] Thus, the secondary nucleation can take place specifically at such defect sites on the preformed crystal surface.[59] The primary building blocks repeatedly grow and attach to the preformed layers, which leads to structure evolution from 2D nanosheets to 3D flower-like structures. As a result, the assembled mesocrystals are more blooming with an increase of particle size and have a number of 3D extended petals. Such curvature formation in ZnNTA is similar to hierarchical structure formation found in biominerals.[58, 59, 61, 62] The internal strain associated with the defects of the attached building blocks increases with an increase of particle size. This enthalpic penalty can be compensated by introducing the misalignment (e.g., curvature) of the outer building blocks, which increases the total entropy of the system and by that the complexity of the biomineral morphologies. Overall, the mesocrystal formation is closely related to its 'primary building block'. The initially formed 2D nanosheet acts as a primary building block which undergoes oriented attachment and mesoscale assembly. The secondary nucleation takes place at the defect sites on the preformed 2D layers. The repeated growth and attachment to the layers lead to formation of 3D flower-like structures.

The flower-like ZnNTA mesocrystals were conformally transformed to hierarchically porous N-doped carbons via pyrolysis ranging from 550 to 1000 °C under $N_2$ gas flow for 2 h with a heating rate of 5 °C min$^{-1}$ without using additional carbon sources. During the pyrolysis, ZnNTAs are converted to the composites of ZnO and polymeric/carbonaceous species at temperature above 400 °C. When the temperature is increased to 800 °C and above, ZnO is carbothermally reduced to Zn metal which can evacuate and be transported away from the carbon with the $N_2$ gas flow (see TGA in **Figure S5**). Four different temperatures of (550, 700, 850, and 1000 °C) were chosen to study the effect of pyrolysis temperature and the method of Zn removal (i.e., by chemical etching and by vaporization) on physicochemical properties (i.e., pore structures, nitrogen content and configuration, as well as degree of graphitization). The resulting samples were labelled as ZnNTA-XE, where X denotes the pyrolysis temperature, and E represents 1 M HCl etching. Zn species in ZnNTA-X are removed by i) HCl etching in ZnNTA-(550E, 700E), ii) combination of vaporization and HCl etching in ZnNTA-850E, and iii) vaporization in ZnNTA-1000. Thus, the role of Zn removal method on the above-mentioned physicochemical properties is investigated.

The characteristic XRD reflections of ZnNTA mesocrystals completely disappear after pyrolysis, which suggest the successful transformation of mesocrystals to the respective ZnO/carbon composites or carbon (**Figure S6**a). ZnNTA-(550 and 700) exhibit sharp reflections that are assigned to the remaining crystalline ZnO. SEM images show highly aggregated ZnO nanocrystals decorating the outer surface of the ZnNTA-(550 and 700) (**Figure S7** and **S8**). TGA under air atmosphere shows that substantial amount of ZnO (ca. 75%) remains in these materials (**Figure S9**). In contrast, ZnNTA-(850, 1000) show neither crystalline ZnO in XRD (Figure S6) nor visible surface aggregates in SEM images (**Figure S10** and **S11**), and exhibit a small ash-content in TGA (Figure S9).

After HCl etching, ZnNTA-XE only exhibit broad (002) diffraction at near 25°, which is typical for disordered amorphous carbon with high surface area (Figure S6b). The diffraction

peaks are slightly stronger in ZnNTA-850E and ZnNTA-1000 due to the increase of graphitic stacking at higher pyrolysis temperature. The absence of crystalline ZnO suggests the successful removal of inorganic species. Inductively coupled plasma-optical emission spectrometry (ICP-OES) confirmed the amount of residual Zn which was in the comparable range of 0.9 ~ 1.2 wt%. ZnNTA-1000 was not treated with HCl because it already had low Zn content (1.2 wt%) after pyrolysis.

The inherent flower morphologies were well conserved without significant structural deformation after carbonization and HCl washing. The highly interconnected hierarchical porous structures with multiple levels of micro/meso/macropores were clearly observed in high-resolution transmission electron microscopy (HRTEM) (**Figure 3**) and SEM images (**Figure S11** and **S12**). Macropores originate from the voids between the intersecting nano/microsheets. HRTEM clearly shows the disordered yet homogeneously distributed mesopores with sizes of 5-20 nm in all samples (Figure 3). ZnNTA-550E has a rather dense morphology with relatively low mesoporosity. Higher pyrolysis temperature leads to the increase of the overall porosity with thinner pore walls, and the gradual development of randomly assembled graphitic layers.

The nitrogen content and its chemical bonding states were analyzed by X-ray photoelectron spectroscopy (XPS). Lower pyrolysis temperature results in higher nitrogen content in ZnNTA-XE, which is in line with the results from elemental analysis (EA) (Table 1). For instance, ZnNTA-550E has the highest nitrogen content of 14.1 at% (XPS) and 10.0 at% (EA). The N1s spectra can be deconvoluted into four component peaks that correspond to pyridinic-N (~398 eV), pyrrolic-N (~400 eV), graphitic-N (~401 eV), and oxidized-N (~403 eV), respectively (**Figure S13**). The relative fractions of pyrrolic- and pyridinic-N decrease while that of graphitic-N increases with increasing the synthesis temperature, because graphitic-N is the most thermally stable N configuration (**Figure S14**). The ongoing development of graphitic carbon with lower N content was also supported by XPS C1s spectra, in which the peaks for graphitic $sp^2$ C=C bonds (~284 eV), N–$sp^2$ C (~285 eV), N–$sp^3$ C (~286 eV), and C-

O bonds (~288 eV) were identified (**Figure S15**).[63] In agreement with the results of the N1s spectra, the contribution from N–sp$^2$ C and N–sp$^3$ C decreases while that of graphitic C=C bonds increases significantly with increasing pyrolysis temperature. Similar changes have been observed in the electron-energy loss spectra (**Figure S16**). The fine structure of the carbon K-edge becomes more pronounced with increasing pyrolysis temperature, while the concentration of nitrogen decreases.

Raman spectroscopy provides additional information about the progress of carbonization at different temperature (**Figure S17**). The D band near ~1355 cm$^{-1}$ arises from the breathing modes of the six-fold sp$^2$ carbon rings in the presence of defects and disorder, while the G-band near ~1600 cm$^{-1}$ originates from the stretching of any pair of sp$^2$ carbons whether in rings or chains. The $I_D/I_G$ peak intensity ratio is commonly used to evaluate the degree of graphitization in porous carbons and is proportional to the amount of sp$^2$ carbon six-rings.[64] In ZnNTA-XEs, the $I_D/I_G$ ratio increases from 0.92 to 1.23 with increasing pyrolysis temperature, indicating that higher temperature treatment leads to aromatization and rearrangements of carbon due to increasing graphitization and the removal of N-containing fragments.[65] The XPS and Raman results show that the properties of ZnNTA-XE carbons such as nitrogen content, nitrogen binding motives, and degree of graphitization can be controlled by adjusting the pyrolysis temperature.

The textural properties of ZnNTA-XE were further characterized by N$_2$ (77 K) physisorption experiments (**Figure 4**; Table 1). N$_2$ physisorption of all ZnNTA-XE results in comparable isotherms, comprising an abrupt N$_2$ uptake at a very low $P/P_0$ <0.05, a continuous slope above $P/P_0$ > 0.1, type H4 hysteresis loop at intermediate $P/P_0$ (0.4-0.95), indicating the presence of hierarchical pore system (Figure 4a).[6] Pore size distributions (PSDs) were estimated by using quenched solid density functional theory (QSDFT) method applied to the adsorption isotherms for N$_2$ adsorbed on carbon with a slit/cylindrical pore shape. ZnNTA-XEs have large specific BET surface area (SSA$_{BET}$) of 970~1605 m$^2$ g$^{-1}$ and high pore volume of

0.95~2.19 cm$^3$ g$^{-1}$, and show rather comparable PSDs with micropores centered at 1.1 nm and broadly distributed mesopores (4-20 nm) centered at 5-8 nm (Figure 4b). With increasing the pyrolysis temperature, the SSA$_{BET}$ and total pore volumes increase significantly to 1605 m$^2$ g$^{-1}$ and 2.19 cm$^3$ g$^{-1}$. The cumulative PSD plots show that the micropores only contribute a small fraction of the total pore volume (especially in the sample ZnNTA-700E), and indicate the drastic increase in mesopore volume for samples heat treated at temperature > 700 °C (Figure 4c). Notably, although ZnNTA-550E has the lowest porosity in general, it shows relatively high micropore volume that is larger than ZnNTA-700E and ZnNTA-850E. The ZnNTA-(700E, 850E, 1000) exhibit comparable mesopore volume yet large difference in micropore volume which increases with an increase of carbonization temperature (Table 1). The substantial increase in micropore volume of ZnNTA-(850E, 1000) is attributed to the carbothermal reduction (ZnO + C → Zn + CO) and subsequent vaporization of in-situ generated Zn metals. Such process works similarly to typical activation processes and preferably occurs with a faster rate at higher temperature, thereby generating a number of micropores in ZnNTA-1000. This is also the reason why the pore walls become thinner and mesopores are slightly increasing in volume and/or size at higher temperature.

To understand the contribution of Zn species to the pore formation, the cumulative PSD plots of ZnNTA-X were gravimetrically normalized by the carbon content, and then compared with those of ZnNTA-XE after HCl etching (**Figure S18**). The overall porosity of ZnNTA-550E is much larger than that of normalized ZnNTA-550 (i.e., there is substantial increase in both micro- and mesoporosity after HCl etching). This result indicates the presence of small Zn clusters and ZnO nanoparticles embedded in the ZnNTA-550 frameworks, which can generate the micropores and mesopores, respectively. In contrast, the overall porosities of ZnNTA-(700E, 850E) and the normalized ZnNTA-(700, 850) are comparable to each other, suggesting that the included ZnO barely contribute to additional pore formation and that the pore structures were already completely developed prior to the removal of ZnO in these materials. The ZnO

nanoparticles were either highly aggregated in ZnNTA-700 (Figure S8) or too low in content to be detected from XRD in ZnNTA-850 (Figure S6).

$CO_2$ and $N_2$ adsorption experiments at 273 K further provide additional information about the narrow pores and the affinity of the materials to the polar $CO_2$ molecules, as well as $CO_2/N_2$ selectivity (Figure 4d). The $CO_2$ uptake of ZnNTA-(550E, 700E, 850E, and 1000) at 273 K and 1 bar was 3.46, 2.59, 3.80, and 4.63 mmol $g^{-1}$, respectively. ZnNTA-1000 with the highest micropore volume shows the largest $CO_2$ uptake because the micropore volume strongly governs the amount of adsorbed $CO_2$.[66] ZnNTA-550E shows a relatively high $CO_2$ uptake, particularly at low pressure of 0.1 bar (1.21 mmol $g^{-1}$).[67] This value is much larger than those of ZnNTA-700E (0.307 mmol $g^{-1}$) and ZnNTA-850E (0.798 mmol $g^{-1}$) and comparable to that of ZnNTA-1000 (1.19 mmol $g^{-1}$), which we attribute to the higher nitrogen content and the smaller micropore diameter in ZnNTA-550E. It is generally believed that the incorporation of nitrogen to the carbon frameworks can increase the polarity of the carbon materials and provide additional $CO_2$ binding sites, thereby leading to significant enhancement in $CO_2$ uptake capacity.[13, 66] The pore diameter also plays a major role for $CO_2$ adsorption accordingly, as pores with sizes of 0.5-0.7 nm or even below (i.e., ultramicropores) can contribute to the amount of adsorbed $CO_2$ more significantly than supermicropores (0.7–2 nm) or mesopores (>2 nm).[67] In contrast to the other samples, ZnNTA-700E shows a distinct hysteresis in the $CO_2$ physisorption isotherm, which is due to its strong $CO_2$ adsorption capability (Figure 4d). This is most likely a result of the combination of high nitrogen content and narrow micropores in this material.

The high $CO_2$ adsorption affinity of ZnNTA-550E is further underlined by investigating the ideal adsorption solution theory (IAST) $CO_2/N_2$ selectivity in comparison to ZnNTA-1000 having the highest $CO_2$ uptake among the samples (**Figure S19**). At 273 K and a $N_2/CO_2$ ratio of 90/10, the selectivity of ZnNTA-550E and ZnNTA-1000 was 43.0 and 19.8, respectively, suggesting the superior $CO_2$ affinity of ZnNTA-550E due to the high nitrogen content and large

(ultra)micropore volume. The selectivity values are not particularly impressive in comparison to the previously reported N-doped carbons, but still suggest the importance of pyrolysis temperature and Zn removal methods on physicochemical properties of the final ZnNTA-XE carbons.

On the basis of aforementioned results, we suggest the possible scenario for the processes of pore formation (**Scheme 2**). The aliphatic NTA ligand itself works as carbon and nitrogen sources and forms random mesopores. The transformation of NTA to organic aggregates and their evaporation possibly occur at a temperature between 400-700 °C (see TGA of Figure S5), leaving numerous sphere-like mesopores in the framework (Figure 3). This result is consistent with previous thermal conversion process of aliphatic carboxylate ligands.[29, 46] Our experimental results also show that mesopores are already formed during the pyrolysis prior to the removal of Zn species (Figure S7-S11). As demonstrated by the relatively high yield and the dense carbon framework morphology (Table 1; Figure 3a), ZnNTA-550 may contain a substantial amount of organic compounds that only can be evaporated at higher temperature. Therefore, the mesopores are more likely to be generated during carbonization > 550 °C, and the ZnNTA-(700E, 850E, and 1000) have rather comparable mesopore volumes regardless of carbonization temperature.

In addition, the in-situ generated Zn species upon pyrolysis also greatly affect the pore structures and diameters, in particular the formation of micropores (Scheme 2). In ZnNTA-550, the Zn ion pairs or small Zn clusters (i.e., embedded $ZnO_x$ clusters) are presumably formed and act as molecular templates generating plenty of (ultra)micropores. The ZnO nanoparticles confined in the carbon matrix can provide additional mesopores whereas those severely aggregated on outer surface cannot contribute to pore generation. In ZnNTA-700, the formation of such surface aggregates is dominant over the others because of higher degree of sintering/aggregation of ZnO nanoparticles at high temperature. Thus, the removal of ZnO rarely generate additional pores and this leads to the lowest microporosity of ZnNTA-700E.

13

However, when the pyrolysis temperature is high enough to induce carbothermal reduction (typically above 800 °C), the in-situ generated Zn metals can produce the new micropores in a similar way to chemical activation. Because of the faster vaporization of Zn metals, ZnNTA-1000 has a higher volume of micropores than ZnNTA-850E. Taking the nonporous nature of ZnNTA mesocrytals into account, the results show that the textural properties of the final carbons are highly dependent on the in-situ generated organic/inorganic pore-forming agents at different carbonization temperature. The results also point out the important perspective that the thermal transformation process and associated pore formation mechanism need to be investigated carefully to prepare the carbons for desired end-uses, as parent precursors with similar structures are transformed to daughter carbons with significantly different physicochemical properties at different pyrolysis temperature.

The present approach is simple, straightforward and does not require time-consuming multi-step processes nor additional sacrificial templates and chemical activation for hierarchical pore formation. Kinetic control of mesocrystal growth enables high level of morphogenesis from 2D nanosheets to 3D flower-like superstructures with controllable particle size and dimension. Controlled pyrolysis and Zn removal lead to preparation of mesocrystal-derived carbon flowers with excellent physicochemical properties superior to those found in previous literature (**Table S1**).

## 3. Conclusion

We have reported the synthesis of 3D flower metal-organic ZnNTA mesocrystals and their conformal transformation to hierarchically porous N-doped carbon via pyrolysis at various temperature (550, 700, 850 and 1000 °C). The 2D ZnNTA nanosheets work as the primary building blocks which align along the common crystallographic basal- and edge-plane via oriented attachment and mesoscale assembly. The secondary nucleation and growth on the edges and defects of preformed layers enable the formation of 3D flower mesocrystals with a

number of extended nanosheets interconnecting each other. The controlled thermal transformation of ZnNTA mesocrystals leads to the formation of carbon flowers with tailored physicochemical properties. The nitrogen content decreases with increasing pyrolysis temperature. The aliphatic NTA ligand forms mesopores and functions as carbon and nitrogen sources. Pyrolysis at 550 °C preferably generates the small Zn clusters leaving a high volume of (ultra)micropores after HCl etching. Higher pyrolysis temperature leads to dominant formation of ZnO aggregates on the external surface which cannot contribute to pore formation in ZnNTA-700. Above 850 °C, in-situ generated Zn metal species act as additional porogens producing numerous micropores via vaporization. Rapid elimination of Zn metal at higher temperature leads to formation of ZnNTA-1000 with the highest micropore content. Benefiting from high N content and the presence of ultramicropores, ZnNTA-550E shows $CO_2/N_2$ selectivity which is twice as high as that of ZnNTA-1000. We demonstrate the use of metal-organic mesocrystals as versatile precursors for unique 3D carbon superstructures that are difficult to access with conventional synthesis methods. The present work provides new insights into the preparation of 3D hierarchical carbon superstructures with tailored physicochemical properties which are highly relevant in a number of potential applications.

## 4. Experimental Section

*Materials*: Concentrated nitric acid ($HNO_3$, 70%, reagent grade, Sigma Aldrich), dimethylformamide (DMF, analytical grade, VWR), nitrilotriacetic acid (NTA, 98%, Sigma Aldrich), and Zn nitrate hexahydrate ($Zn(NO_3)_2 \cdot 6H_2O$, 98%, Alfa Aesar) were used as received.

*Synthesis of ZnNTA mesocrystals*: For synthesis of flower-like ZnNTA mesocrystals, a solution of $Zn(NO_3)_2$ $6H_2O$ (1.92 mmol, 571 mg) in DMF (15 ml) was added to a solution of NTA (1.28 mmol, 245 mg) and $HNO_3$ (3.84 mmol, 243 μL) in DMF (15 ml). The transparent, homogenous mixture was heated in a Teflon-lined autoclave at 120 °C for 24 h, and then cooled down to

ambient temperature. The crystalline precipitates were washed with DMF for 3 times, followed by drying under reduced pressure for 24 h at 85 °C.

*ZnNTA mesocrystals derived N-doped hierarchically porous carbons (ZnNTA-x)*: As-made ZnNTA mesocrystals were carbonized at 550, 700, 850 and 1000 °C for 2 h under $N_2$ flow in a horizontal tubular furnace with a heating rate of 5 °C min$^{-1}$. To remove ZnO, ZnNTA-(550, 700, 850) were immersed in 1 M HCl under gentle stirring overnight and washed with Milli-Q water repeatedly, followed by drying under a reduced pressure for 24 h at 85 °C.

*Characterizations*: X-ray powder diffraction (XRD) was recorded on a Bruker D8 Advance diffractometer equipped with a scintillation counter detector (KeveX Detector) with Cu-Kα radiation ($\lambda$ = 0.154 nm). $N_2$ adsorption and desorption experiments were performed using Quantachrome Quadrasorb apparatus at 77 K. The samples were degassed at 150 °C for 20 h before measurements and analyzed with the QuadraWin software (version 5.05). The SSAs were calculated by the multipoint Brunauer–Emmett–Teller (BET) model ($P/P_0$ = 0.05–0.2). Total pore volumes ($V_t$) were determined at $P/P_0$ = 0.95. PSDs were calculated using quenched solid density functional theory (QSDFT) method (adsorption branch kernel) for $N_2$ adsorbed on carbon with a slit/cylindrical pore shape at 77 K. Micropore volumes given in Table 1 was the cumulative pore volume at 2 nm determined by the QSDFT method. $CO_2$ physisorption experiments were carried out at 273 K on the Quantachrome Autosorb IQ apparatus. The determination of $CO_2$ over $N_2$ selectivity (S) (at 273 K; for $N_2/CO_2$ ratio of 90/10) followed the ideal adsorption solution theory (IAST) method and was calculated using following equation:

$$S_{CO_2/N_2} = \left. X_{CO_2} \middle/ X_{N_2} \right. \times \left. Y_{N_2} \middle/ Y_{CO_2} \right.$$

where $X$ is the molar ratio of $CO_2$ or $N_2$ in the adsorbed phase and $Y$ is the molar ratio in the gas phase. Inductively coupled plasma-optical emission spectrometry (ICP-OES) was conducted using a PerkinElmer Optima 8000 instrument, calibrated with standard solutions. For high-resolution transmission electron microscopy (HRTEM) observations, a suspension of the

sample in ethanol was sonicated for 10 minutes and then drop-casted to a Cu grid with a lacey carbon support and dried for 5 minutes. The HRTEM study was performed using a double Cs corrected JEOL JEM-ARM200F (S)TEM operated at 80kV, equipped with a cold-field emission gun and a Gatan Quantum GIF spectroscopy system. All electron energy loss spectra have been collected at dispersion of 0.1eV/ch. Scanning electron microscopy (SEM) was performed on a Zeiss LEO 1550 microscope operating at 3.0 kV. Thermogravimetric analysis (TGA) was conducted with a Netzsch TG 209 F1 device under constant nitrogen or artificial air flow in platinum pans at a heating rate of 10 °C min$^{-1}$ to 1000 °C. Elemental analysis was performed with a vario MICRO cube CHNOS Elemental Analyzer in the CHNS mode. The deviation for the estimated EA values were less than 0.30%. X-ray photoelectron spectroscopy (XPS) measurements were performed using a Thermo Scientific K-Alpha+ X-ray Photoelectron Spectrometer. Elemental compositions were determined using survey scans over a range of 1350–0 eV with a step size of 1.0 eV and a pass energy of 200 eV. Raman spectra were recorded using a LabRam Aramis (Horiba Jobin Yvon) Raman microscope operating with an objective (x100, spot size ~1 um) and a 514 nm Ar-ion laser (power on sample of 1 mW).

**Supporting Information**
Supporting Information is available from the Wiley Online Library or from the author.

**References**

[1]     M.-H. Sun, S.-Z. Huang, L.-H. Chen, Y. Li, X.-Y. Yang, Z.-Y. Yuan, B.-L. Su, *Chem. Soc. Rev.* **2016,** *45*, 3479.
[2]     J. Lee, J. Kim, T. Hyeon, *Adv. Mater.* **2006,** *18*, 2073.
[3]     D. Yu, K. Goh, H. Wang, L. Wei, W. Jiang, Q. Zhang, L. Dai, Y. Chen, *Nat. Nanotechnol.* **2014,** *9*, 555.
[4]     Z. Li, Z. Liu, H. Sun, C. Gao, *Chem. Rev.* **2015,** *115*, 7046.
[5]     E. V. Sturm, H. Cölfen, *Chem. Soc. Rev.* **2016,** *45*, 5821.

[6]     K. A. Cychosz, R. Guillet-Nicolas, J. García-Martínez, M. Thommes, *Chem. Soc. Rev.* **2017,** *46*, 389.

[7]     J. Hwang, C. Jo, K. Hur, J. Lim, S. Kim, J. Lee, *J. Am. Chem. Soc.* **2014,** *136*, 16066.

[8]     C. Jo, J. Hwang, W.-G. Lim, J. Lim, K. Hur, J. Lee, *Adv. Mater.* **2018,** *30*, 1703829.

[9]     S. Dutta, A. Bhaumik, K. C. W. Wu, *Energy Environ. Sci.* **2014,** *7*, 3574.

[10]     C. M. Parlett, K. Wilson, A. F. Lee, *Chem. Soc. Rev.* **2013,** *42*, 3876.

[11]     M. Oschatz, L. Borchardt, M. Thommes, K. A. Cychosz, I. Senkovska, N. Klein, R. Frind, M. Leistner, V. Presser, Y. Gogotsi, S. Kaskel, *Angew. Chem., Int. Ed.* **2012,** *51*, 7577.

[12]     J. Hwang, S. Kim, U. Wiesner, J. Lee, *Adv. Mater.* **2018,** *30*, 1801127.

[13]     R. Walczak, B. Kurpil, A. Savateev, T. Heir, J. Schmidt, Q. Qin, M. Antonietti, M. Oschatz, *Angew. Chem., Int. Ed.* **2018,** *57*, 10765.

[14]     Z.-S. Wu, Y. Sun, Y.-Z. Tan, S. Yang, X. Feng, K. Müllen, *J. Am. Chem. Soc.* **2012,** *134*, 19532.

[15]     Z. Xu, X. Zhuang, C. Yang, J. Cao, Z. Yao, Y. Tang, J. Jiang, D. Wu, X. Feng, *Adv. Mater.* **2016,** *28*, 1981.

[16]     D. Guo, H. Wei, X. Chen, M. Liu, F. Ding, Z. Yang, Y. Yang, S. Wang, K. Yang, S. Huang, *J. Mater. Chem. A* **2017,** *5*, 18193.

[17]     J. Liang, S. Chen, M. Xie, Y. Wang, X. Guo, X. Guo, W. Ding, *J. Mater. Chem. A* **2014,** *2*, 16884.

[18]     Q. Wang, J. Yan, Y. Wang, T. Wei, M. Zhang, X. Jing, Z. Fan, *Carbon* **2014,** *67*, 119.

[19]     L. Zhou, T. Huang, A. Yu, *ACS Sus. Chem. Eng.* **2014,** *2*, 2442.

[20]     S. Chen, D. M. Koshy, Y. Tsao, R. Pfattner, X. Yan, D. Feng, Z. Bao, *J. Am. Chem. Soc.* **2018,** *140*, 10297.

[21]     J. Zhang, M. Lv, D. Liu, L. Du, Z. Liang, *Int. J. Hydrogen Energy* **2018,** *43*, 4311.

[22]     W. Liu, M. Zhu, B. Dai, *New J. Chem.* **2018,** *42*, 20131.

[23]     H. Tian, N. Wang, F. Xu, P. Zhang, D. Hou, Y. Mai, X. Feng, *J. Mater. Chem. A* **2018,** *6*, 10354.

[24]     G. Zhao, G. Zou, X. Qiu, S. Li, T. Guo, H. Hou, X. Ji, *Electrochim. Acta* **2017,** *240*, 24.

[25]     N. D. Petkovich, A. Stein, *Chem. Soc. Rev.* **2013,** *42*, 3721.

[26]     S. Kubo, R. J. White, K. Tauer, M.-M. Titirici, *Chem. Mater.* **2013,** *25*, 4781.

[27]     A. Ahmadpour, D. Do, *Carbon* **1996,** *34*, 471.

[28]     M. Chen, Y. Zhang, L. Xing, Y. Liao, Y. Qiu, S. Yang, W. Li, *Adv. Mater.* **2017,** *29*, 1607015.

[29]     K. J. Lee, J. H. Lee, S. Jeoung, H. R. Moon, *Acc. Chem. Res.* **2017,** *50*, 2684.

[30]     M. Oschatz, S. Krause, N. A. Krans, C. Hernández Mejía, S. Kaskel, K. P. de Jong, *Chem.Commun.* **2017,** *53*, 10204.

[31]     Y. V. Kaneti, J. Tang, R. R. Salunkhe, X. Jiang, A. Yu, K. C. W. Wu, Y. Yamauchi, *Adv. Mater.* **2017,** *29*, 1604898.

[32]     H.-C. Lee, J. Hwang, U. Schilde, M. Antonietti, K. Matyjaszewski, B. V. K. J. Schmidt, *Chem. Mater.* **2018,** *30*, 2983.

[33]     H.-C. Lee, M. Fantin, M. Antonietti, K. Matyjaszewski, B. V. K. J. Schmidt, *Chem. Mater.* **2017,** *29*, 9445.

[34]     J. Hwang, H.-C. Lee, M. Antonietti, B. V. K. J. Schmidt, *Polym. Chem.* **2017,** *8*, 6204.

[35]     S. Dang, Q.-L. Zhu, Q. Xu, *Nat. Rev. Mater.* **2017,** *3*, 17075.

[36]     M. Lismont, L. Dreesen, S. Wuttke, *Adv. Funct. Mater.* **2017,** *27*, 1606314.

[37]     H.-C. Lee, T. Heil, J.-K. Sun, B. V. K. J. Schmidt, *Mater. Horiz.* **2019,** *6*, 802.

[38]     M. Hu, J. Reboul, S. Furukawa, N. L. Torad, Q. Ji, P. Srinivasu, K. Ariga, S. Kitagawa, Y. Yamauchi, *J. Am. Chem. Soc.* **2012,** *134*, 2864.

[39]     J. Hwang, R. Yan, M. Oschatz, B. V. K. J. Schmidt, *J. Mater. Chem. A* **2018,** *6*, 23521.

[40]    B. Liu, H. Shioyama, T. Akita, Q. Xu, *J. Am. Chem. Soc.* **2008,** *130*, 5390.

[41]    X. Zhao, H. Yang, P. Jing, W. Shi, G. Yang, P. Cheng, *Small* **2017,** *13*, 1603279.

[42]    Y.-H. Shih, C.-P. Fu, W.-L. Liu, C.-H. Lin, H.-Y. Huang, S. Ma, *Small* **2016,** *12*, 2057.

[43]    W. Chaikittisilp, K. Ariga, Y. Yamauchi, *J. Mater. Chem. A* **2013,** *1*, 14.

[44]    Z. Li, X. Liu, L. Wang, F. Bu, J. Wei, D. Pan, M. Wu, *Small* **2018,** *14*, 1801498.

[45]    L. Zhang, Y. H. Hu, *J. Phys, Chem. C* **2010,** *114*, 2566.

[46]    T. K. Kim, K. J. Lee, J. Y. Cheon, J. H. Lee, S. H. Joo, H. R. Moon, *J. Am. Chem. Soc.* **2013,** *135*, 8940.

[47]    S. Lim, K. Suh, Y. Kim, M. Yoon, H. Park, D. N. Dybtsev, K. Kim, *Chem. Commun.* **2012,** *48*, 7447.

[48]    S. J. Yang, T. Kim, J. H. Im, Y. S. Kim, K. Lee, H. Jung, C. R. Park, *Chem. Mater.* **2012,** *24*, 464.

[49]    J. Hwang, T. Heil, M. Antonietti, B. V. K. J. Schmidt, *J. Am. Chem. Soc.* **2018,** *140*, 2947.

[50]    L. Bergström, E. V. Sturm, G. Salazar-Alvarez, H. Cölfen, *Acc. Chem. Res.* **2015,** *48*, 1391.

[51]    J. Popovic, R. Demir-Cakan, J. Tornow, M. Morcrette, D. S. Su, R. Schlögl, M. Antonietti, M.-M. Titirici, *Small* **2011,** *7*, 1127.

[52]    P. Zhang, H. Li, G. M. Veith, S. Dai, *Adv. Mater.* **2015,** *27*, 234.

[53]    S. J. Yang, M. Antonietti, N. Fechler, *J. Am. Chem. Soc.* **2015,** *137*, 8269.

[54]    J. Wei, Y. Liang, Y. Hu, B. Kong, J. Zhang, Q. Gu, Y. Tong, X. Wang, S. P. Jiang, H. Wang, *Angew. Chem., Int. Ed.* **2016,** *55*, 12470.

[55]    H. Ejima, J. J. Richardson, K. Liang, J. P. Best, M. P. van Koeverden, G. K. Such, J. Cui, F. Caruso, *Science* **2013,** *341*, 154.

[56]    T. Egli, *J. Biosci. Bioeng.* **2001,** *92*, 89.

[57]    X.-Q. Lü, J.-J. Jiang, C.-L. Chen, B.-S. Kang, C.-Y. Su, *Inorg. Chem.* **2005,** *44*, 4515.

[58]    F. C. Meldrum, H. Cölfen, *Chem. Rev.* **2008,** *108*, 4332.

[59]    H. Cölfen, S. Mann, *Angew. Chem., Int. Ed.* **2003,** *42*, 2350.

[60]    R. L. Penn, J. F. Banfield, *Science* **1998,** *281*, 969.

[61]    R. Kniep, P. Simon, *Angew. Chem., Int. Ed.* **2008,** *47*, 1405.

[62]    S. Busch, H. Dolhaine, A. DuChesne, S. Heinz, O. Hochrein, F. Laeri, O. Podebrad, U. Vietze, T. Weiland, R. Kniep, *Eur. J. Inorg. Chem.* **1999,** *10*, 1643.

[63]    H. Wang, T. Maiyalagan, X. Wang, *ACS Catal.* **2012,** *2*, 781.

[64]    A. Ferrari, J. Robertson, *Phys. Rev. B* **2000,** *61*, 14095.

[65]    T. P. Fellinger, A. Thomas, J. Yuan, M. Antonietti, *Adv. Mater.* **2013,** *25*, 5838.

[66]    M. Oschatz, M. Antonietti, *Energy Environ. Sci.* **2018,** *11*, 57.

[67]    V. Presser, J. McDonough, S.-H. Yeon, Y. Gogotsi, *Energy Environ. Sci.* **2011,** *4*, 3059.
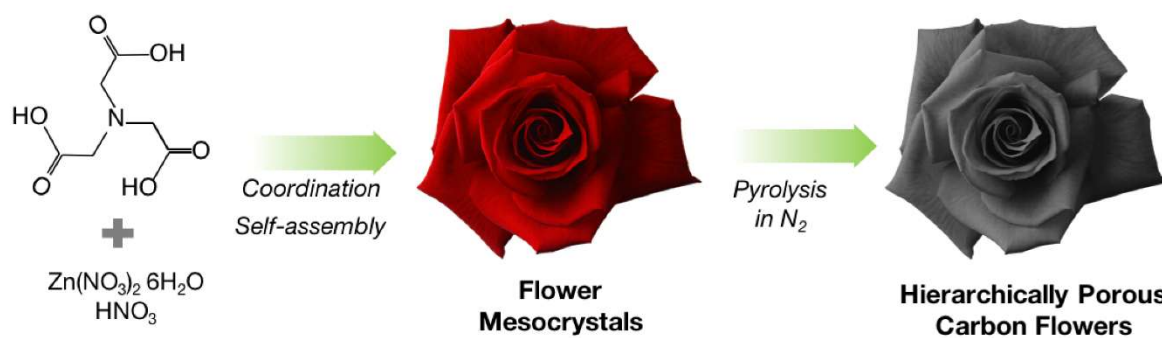
**Scheme 1.** Synthesis of flower-like ZnNTA mesocrystals and their conformal transformation to hierarchically porous N-doped carbon flowers.
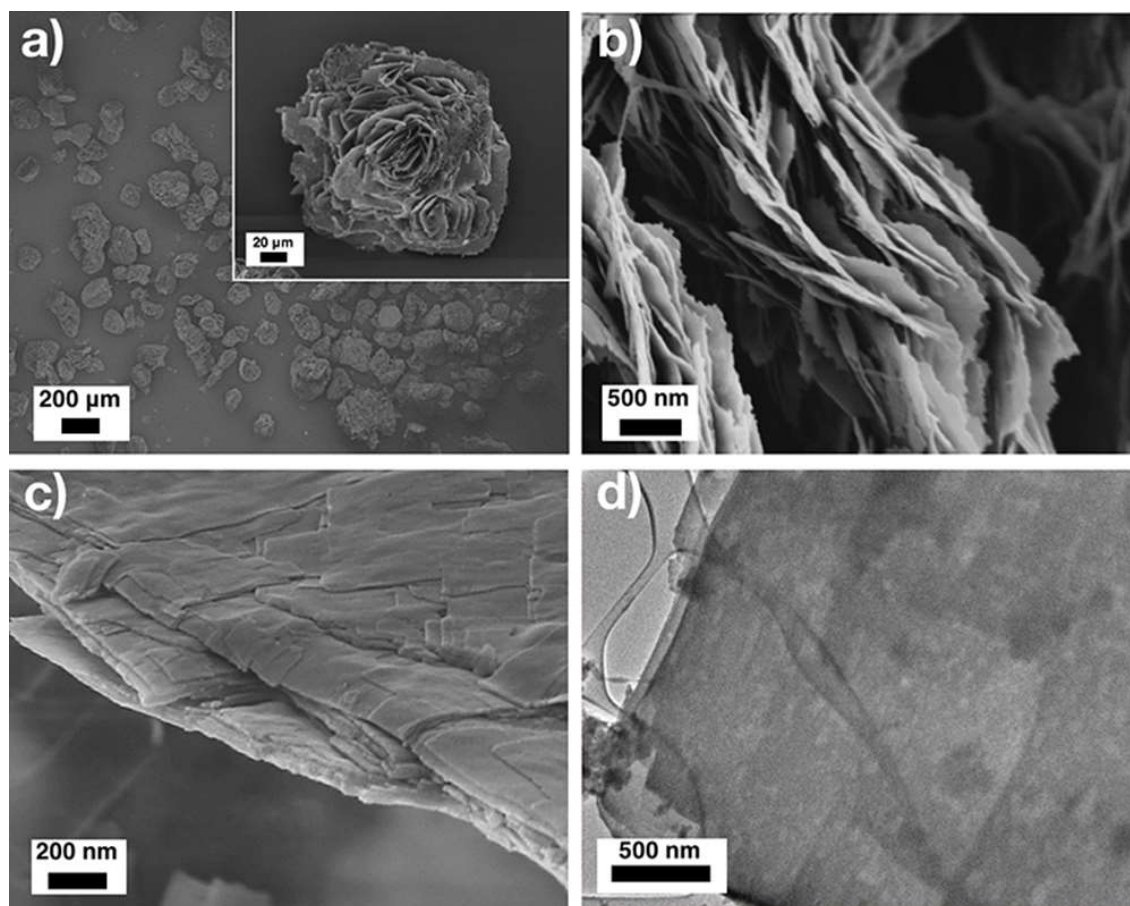


**Figure 1.** SEM and TEM images of Flower-like ZnNTA mesocrystals (a), and intersecting micropetals comprised of 2D nanosheets (b, c). TEM image of exfoliated mesocrystals (d). ZnNTA mesocrystals were prepared with the molar ratios of Zn/NTA = 1.5 and HNO$_3$/NTA = 3.
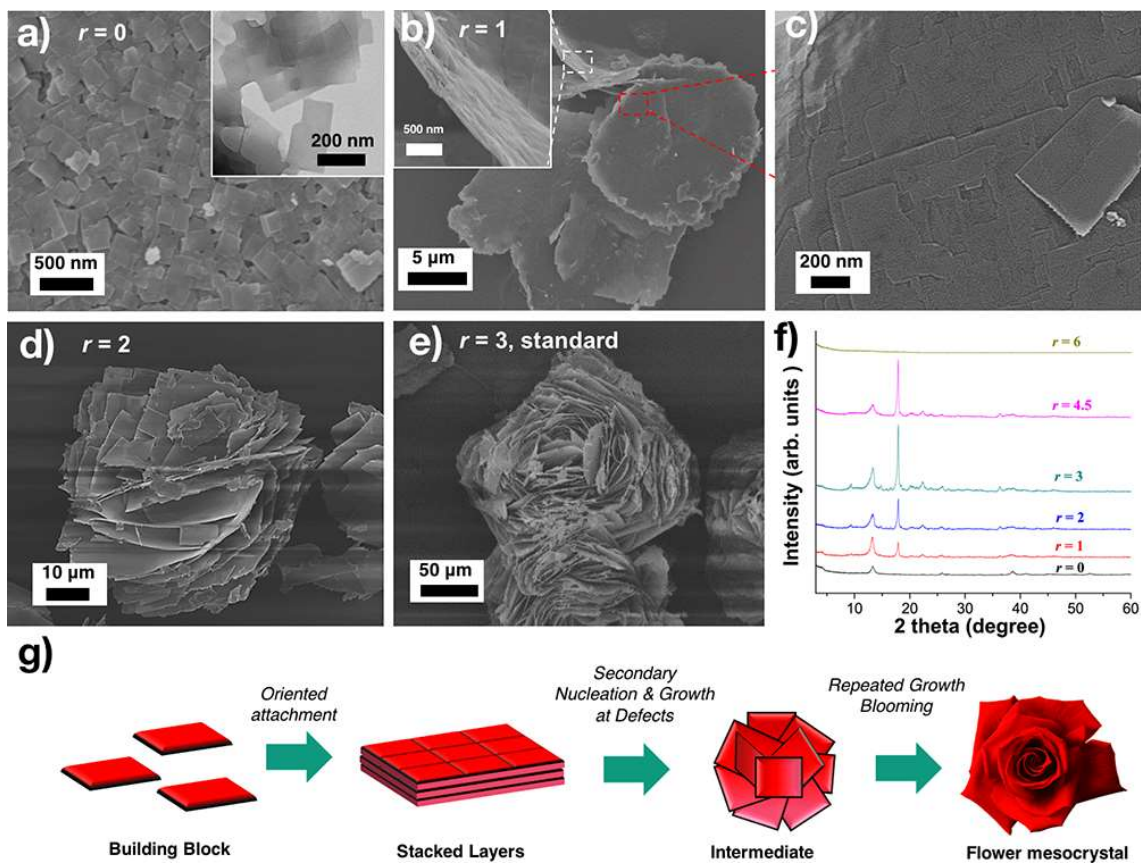
**Figure 2.** Kinetically controlled growth of ZnNTA mesocrystals prepared with different HNO$_3$/NTA ratio ($r$). SEM images of ZnNTA at (a) $r = 0$, (b, c) $r = 1$, (d) $r = 2$, and (e) $r = 3$. (f) XRD patterns of ZnNTA. (g) Suggested formation mechanism of flower mesocrystals.
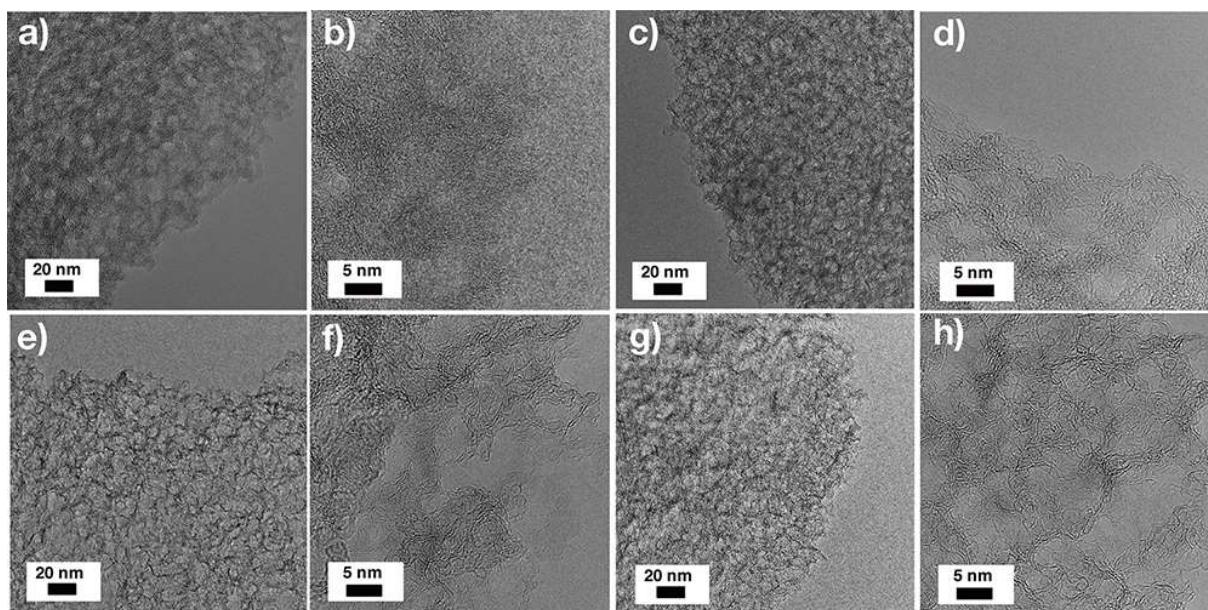
**Figure 3.** HRTEM images of ZnNTA-550E (a, b), ZnNTA-700E (c, d), ZnNTA-850E (e, f) and ZnNTA-1000 (g, h).
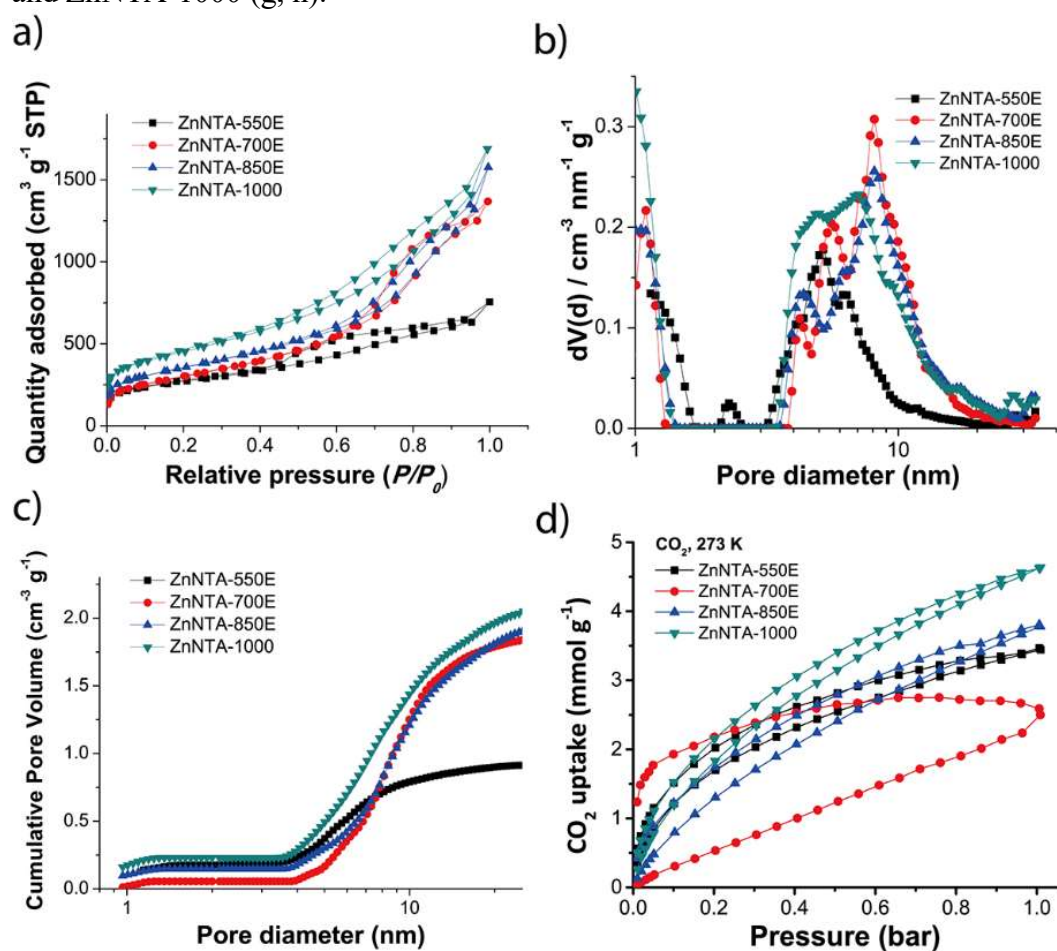


**Figure 4.** $N_2$ physisorption isotherms at 77K (a) and corresponding differential (b) and cumulative QSDFT PSD (c). $CO_2$ physisorption isotherms at 273K (d).

**Table 1.** Physisorption, Raman spectroscopy, EA, and XPS data summary as well as yield of flower shaped hierarchically porous carbons derived from ZnNTA mesocrystals.

| Samples | SSA [a] $[m^2\,g^{-1}]$ | $V_{micro}$ [b] $[cm^3\,g^{-1}]$ | $V_{meso}$ [c] $[cm^3\,g^{-1}]$ | $V_{total}$ [d] $[cm^3\,g^{-1}]$ | $I_D/I_G$ | Nitrogen | | Yield [%] |
|---|---|---|---|---|---|---|---|---|
| | | | | | | EA [at%] | XPS [at%] | |
| ZnNTA-550E | 970 | 0.18 | 0.77 | 0.95 | 0.92 | 10.0 | 14.1 | 14.5 |
| ZnNTA-700E | 1090 | 0.06 | 1.88 | 1.94 | 1.16 | 9.5 | 13.8 | 7.5 |
| ZnNTA-850E | 1260 | 0.15 | 1.89 | 2.04 | 1.20 | 3.4 | 6.5 | 3.6 |
| ZnNTA-1000 | 1605 | 0.27 | 1.92 | 2.19 | 1.23 | 3.0 | 3.4 | 3.5 |

[a] Determined by multipoint BET method ($P/P_0 = 0.05$–$0.2$).; [b] The cumulative pore volume at 2 nm determined by the QSDFT method for $N_2$ adsorbed on carbon at 77 K. [c] $V_{total}$-$V_{micro}$ [d] Determined at $P/P_0 = 0.95$.
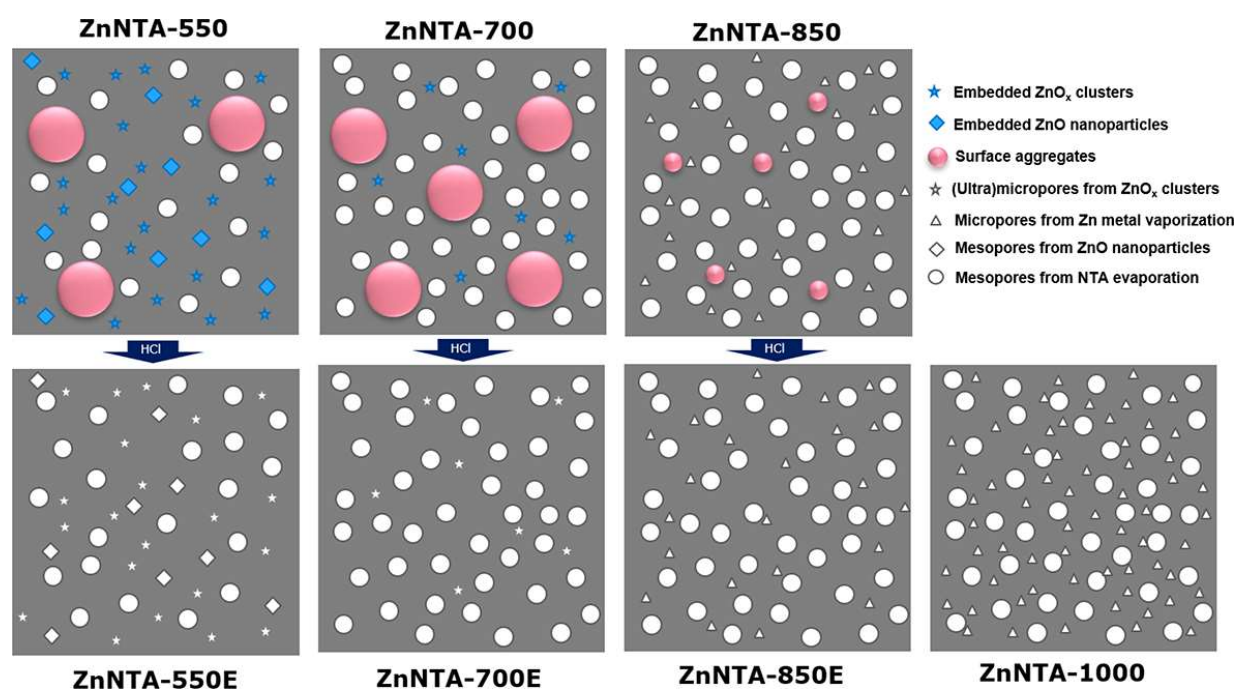


**Scheme 2.** Illustration of the effect of pyrolysis temperature and removal of in-situ generated Zn species on textural properties of carbons derived from ZnNTA mesocrystals.

**Metal-organic mesocrystals with 3D flower-like superstructures** are solvothermally synthesized and employed as versatile precursors for hierarchically porous nitrogen doped carbon with flower-like appearance that is difficult to access through conventional synthesis methods. The control over pyrolysis temperature and associated in-situ generation of porogens lead to high nitrogen content and (ultra)micropores which increase the $CO_2/N_2$ selectivity significantly.

**Keyword** metal-organic mesocrystals, 3D flowers, hierarchically porous carbon, thermal transformation mechanism

Jongkook Hwang, Ralf Walczak, Martin Oschatz, Nadezda V. Tarakina, and Bernhard V. K. J. Schmidt *

**Micro-Blooming: Hierarchically Porous Nitrogen-doped Carbon Flowers derived from Metal-Organic Mesocrystals**

ToC figure